

Open Research Online

The Open University's repository of research publications
and other research outputs

Molecular clumps in the W51 giant molecular cloud

Journal Item

How to cite:

Parsons, H.; Thompson, M. A.; Clark, J. S. and Chrysostomou, A. (2012). Molecular clumps in the W51 giant molecular cloud. *Monthly Notices of the Royal Astronomical Society*, 424(3) pp. 1658–1671.

For guidance on citations see [FAQs](#).

© 2012 The Authors; 2012 RAS (Monthly Notices of the Royal Astronomical Society)

Version: Version of Record

Link(s) to article on publisher's website:

<http://dx.doi.org/doi:10.1111/j.1365-2966.2012.21106.x>

Copyright and Moral Rights for the articles on this site are retained by the individual authors and/or other copyright owners. For more information on Open Research Online's data [policy](#) on reuse of materials please consult the policies page.

oro.open.ac.uk

Molecular clumps in the W51 giant molecular cloud

H. Parsons,^{1,2*} M. A. Thompson,^{1*} J. S. Clark³ and A. Chrysostomou^{1,2}

¹Centre for Astrophysics Research, Science & Technology Research Institute, University of Hertfordshire, College Lane, Hatfield AL10 9AB

²Joint Astronomy Centre, 660 North A'ohoku Place, University Park, Hilo, HI 96720, USA

³Department of Physics and Astronomy, The Open University, Walton Hall, Milton Keynes MK7 6AA

Accepted 2012 April 10. Received 2012 April 9; in original form 2011 December 16

ABSTRACT

In this paper, we present a catalogue of dense molecular clumps located within the W51 giant molecular cloud (GMC). This work is based on Heterodyne Array Receiver Programme $^{13}\text{CO } J = 3-2$ observations of the W51 GMC and uses the automated CLUMPFIND algorithm to decompose the region into a total of 1575 clumps of which 1130 are associated with the W51 GMC. We clearly see the distinct structures of the W51 complex and the high-velocity stream previously reported. We find the clumps have characteristic diameters of 1.4 pc, excitation temperatures of 12 K, densities of $5.6 \times 10^{21} \text{ cm}^{-2}$, surface densities 0.02 g cm^{-2} and masses of $90 M_{\odot}$. We find a total mass of dense clumps within the GMC of $1.5 \times 10^5 M_{\odot}$, with only 1 per cent of the clumps detected by number and 4 per cent by mass found to be supercritical. We find a clump-forming efficiency of 14 ± 1 per cent for the W51 GMC and a supercritical clump-forming efficiency of $0.5^{+2.3}_{-0.5}$ per cent. Looking at the clump mass distribution, we find it is described by a single power law with a slope of $\alpha = 2.4^{+0.2}_{-0.1}$ above $\sim 100 M_{\odot}$. By comparing locations of supercritical clumps and young clusters, we see that any future star formation is likely to be located away from the currently active W51A region.

Key words: molecular data – catalogues – stars: formation – ISM: clouds – submillimetre: ISM.

1 INTRODUCTION

Massive stars are known to form in giant molecular clouds (GMCs) found throughout the Galaxy. However, despite the importance of GMCs in the early stages of massive star formation, a number of questions still remain: it is not clear how star formation propagates through the natal GMC and, in particular, the role the first generation of massive stars plays in triggering, regulating and terminating subsequent activity. Additionally, the processes governing the fragmentation of the GMC and the subsequent assemblage of stars and stellar clusters are uncertain, with several different mechanisms proposed to accomplish this (e.g. Bonnell, Bate & Zinnecker 1998; Yorke & Sonnhalter 2002; Bonnell & Bate 2006).

In this paper, we focus on the W51 GMC located in the Sagittarius arm of the Galaxy. Originally identified by Westerhout (1958) from 21 cm continuum emission, the W51 GMC is one of the most active and massive star-forming regions in the Galaxy; it is in the top 1 per cent of GMCs by size and upper 5–10 per cent by mass (Carpenter & Sanders 1998). It has a high star-forming efficiency (SFE) of 5–15 per cent (Koo 1999; Kumar, Kamath & Davis 2004) and

has a starburst-like star formation history with the majority of the star formation in the W51 GMC occurring within the past ~ 3 Myr (Okumura et al. 2000; Kumar et al. 2004; Clark et al. 2009). The W51 GMC comprises multiple H II regions (Koo 1999) and exciting star clusters (Kumar et al. 2004), all of which are embedded in the natal material. Near-infrared spectroscopy has revealed the presence of a number of apparently recently formed O stars within at least one region of the GMC (Okumura et al. 2000; Figuerêdo et al. 2008). Mid-infrared observations reveal the presence of a third generation of massive protostars associated with the W51 GMC (Kang et al. 2009), while maser, molecular and submillimetre observations reveal even younger populations of massive protostellar objects (e.g. Zapata et al. 2009; Shi, Zhao & Han 2010).

To date, molecular observations of the W51 GMC, needed to investigate the earliest stages of star formation, are predominantly for the ground states of ^{12}CO and ^{13}CO , tracing the extended emission within the complex at low angular resolution [Koo (1999): $^{12}\text{CO } (J = 2-1)$ and $(J = 1-0)$; Carpenter & Sanders (1998): $^{12}\text{CO } (J = 1-0)$ and $^{13}\text{CO } (J = 1-0)$; Kang et al. (2010): $^{12}\text{CO } (J = 2-1)$ and $^{13}\text{CO } (J = 2-1)$]. Although some higher angular resolution observations (again of the ground state of ^{13}CO) have been made, these have been over smaller regions, typically surrounding one of the known H II regions within the W51 GMC (Koo 1999; Okumura et al. 2001; Sollins, Zhang & Ho 2004). Observations of

*E-mail: h.parsons@jach.hawaii.edu (HP); M.A.Thompson@herts.ac.uk (MAT)

this type are crucial to trace the molecular content of the complex before any massive young stellar objects have had enough time and energy to ionize their surrounding material, making them visible in the infrared. This is the material responsible for star formation in the W51 GMC and so a detailed analysis of the location and state of this reservoir is needed for understanding this giant complex. In this paper, we present new high resolution and signal-to-noise ratio (S/N) molecular observations of the entire complex.

We present the overall extent and morphology of the W51 GMC, utilizing the radial velocity data to decompose it into its constituent parts. We present a catalogue of molecular clumps within the complex, which we further characterize in terms of opacity, temperature, geometric size, mass and density. This in turn yields a measure of the total mass of the GMC contained within clumps, the reservoir of dense material available for star formation, as well as locating clumps with respect to past and current activity. Finally, we construct a clump mass function, for comparison to other mass function within the W51 GMC and also to other low- and high-mass star-forming regions such as Orion (Nutter & Ward-Thompson 2007; Buckle et al. 2010), M17 (Reid & Wilson 2006a) and W3 (Moore et al. 2007).

2 OBSERVATIONS AND DATA REDUCTION

2.1 Observations

The W51 GMC was mapped using the Heterodyne Array Receiver Programme (HARP) receiver with the back-end digital autocorrelator spectrometer Auto-Correlation Spectral Imaging System (ACSIS) on the James Clerk Maxwell Telescope (JCMT).

HARP has 16 SIS receptors that operate between 325 and 375 GHz. The receptors are arranged in a 4×4 array separated by 30 arcsec, with a beam size of 14 arcsec, which means the sky is undersampled (Buckle et al. 2009). HARP has several observing modes to account for this with rastering as the most efficient technique to cover a large region such as the W51 GMC. This involves rotating the k -mirror so that the array is at an angle of 14.48 with respect to the scan direction, allowing for a fully sampled image. The area mapped by HARP was covered by a minimum of two repeats, with perpendicular scan directions, in order to build up signal and minimize sky and system uncertainties: a technique known as ‘basket weaving’. The large extent of the W51 GMC required the region to be split into 13 submaps typically 1020×1020 arcsec² in size, observed with a scan spacing of 1/2 an array (58.2 arcsec).

The data, taken in 2008 May, comprise ~ 36 h observing time taken in grade 2/3 weather (0.05 – $0.12 \tau_{225 \text{ GHz}}$, where $\tau_{225 \text{ GHz}}$ is the sky opacity at 225 GHz, as measured by the Caltech Submillimeter Observatory radiometer). Observations of ^{13}CO and C^{18}O in the $J = 3$ – 2 transition were obtained simultaneously using the multi-subsystem mode of ACSIS, as were ^{12}CO ($J = 3$ – 2) and H^{13}CO^+ ($J = 4$ – 3) in a separate tuning. In this paper, we focus entirely upon the ^{13}CO and C^{18}O data. We will present the ^{12}CO data in a forthcoming paper on the distribution of molecular outflows within W51. As the H^{13}CO^+ observations were acquired simultaneously to the ^{12}CO observations, the resulting short integration times required to detect ^{12}CO were inadequate to detect H^{13}CO^+ towards more than a few positions. A band width of 250 MHz was chosen for the observations, with a spectral resolution of 61 kHz, providing a velocity resolution of 0.08 km s^{-1} . After an initial check of three potential sites, the reference position was chosen for all observations: $19^{\text{h}}18^{\text{m}}03^{\text{s}}.8, +14^{\circ}01'53''$.

2.2 Data reduction

The raw data from HARP/ACSIS consist of a number of time series cubes, where data are ordered by receptor, time and velocity. The data were reduced using the automated astronomical data reduction pipeline: ORAC-DR (Cavanagh et al. 2008).

ORAC-DR takes each raw time series in a set of observations and creates a position–position–velocity cube. ORAC-DR then does quality assurance (QA) against specific requirements that may be user defined. The QA checks include comparing individual and mean system temperatures and rms values, and a comparison of system temperatures on a spectrum-by-spectrum basis. These QA parameters are the same as those used by the Gould Belt Survey (GBS;¹ Ward-Thompson et al. 2007). Receptors that violate the QA are set to ‘bad’. ORAC-DR also removes gross features and any time variations. A baseline is created by smoothing the raw data from each observation in spatial and frequency coordinates. Once applied, the spatial uniformity and rms with respect to frequency are checked over the central 50 per cent of the map. This baseline is removed from the raw data and the method is repeated. Finally, the data are regridded into RA, Dec. and velocity cubes.

To convert between the antenna temperature and the receiver temperature, T_{R} , a main beam efficiency of $\eta_{\text{mb}} = 0.63$ was used² for all the isotopologues. The reduced submaps were then combined in a mosaic using the nearest neighbour algorithm (chosen to prevent further smoothing of the data, which is defined as assigning the input pixel value completely to the single nearest output pixel³). The final image has an angular resolution of 14 arcsec, a pixel scale of 7.3 arcsec; the data were also rebinned in velocity to a 0.5 km s^{-1} channel width to improve S/N. We investigated using CLUMPFIND on the native 0.1 km s^{-1} resolution data cubes and found that at this velocity resolution CLUMPFIND tends to artificially fragment clumps into a main clump surrounded by unphysical low linewidth fragments occupying only a few pixels each. This may be due to S/N effects in the lower S/N outskirts of the clumps. Inspecting the integrated velocity-weighted dispersion image of the ^{13}CO data cube shows that the bulk of the emission has a linewidth in excess of 0.5 km s^{-1} and so we chose to bin our data cubes to this velocity resolution. At a resolution of 0.5 km s^{-1} , the clump fragmenting effect is largely eliminated. The final three-colour integrated intensity image produced using ^{12}CO , ^{13}CO and C^{18}O is seen in Fig. 1 with the final median rms across the area mapped being 0.6, 0.4 and 0.5 K for ^{12}CO , ^{13}CO and C^{18}O , respectively. The data presented in this paper are available in their raw form via the CADC⁴ JCMT Science Archive. The reduced data are available upon request.

2.3 Clump identification

The clump catalogue produced in this paper is created from the ^{13}CO $J = 3$ – 2 data cubes. ^{13}CO $J = 3$ – 2 is used as it traces the warm dense gas and is less optically thick than ^{12}CO $J = 3$ – 2 , which as a result is limited to tracing the outer envelope of the W51 GMC. In contrast to C^{18}O $J = 3$ – 2 , ^{13}CO is brighter. Molecular clouds have a hierarchical internal structure comprised of clumps

¹ For a description of the QA parameters as well as those used by the GBS, see www.jach.hawaii.edu/JCMT/surveys/docs/QA_v1.0.pdf

² www.jach.hawaii.edu/JCMT/spectral_line/General/status.html

³ <http://starlink.jach.hawaii.edu/starlink>

⁴ The Canadian Astronomy Data Centre: www.cadc-ccda.hia-ihp.nrc-cnrc.gc.ca/cadc/.

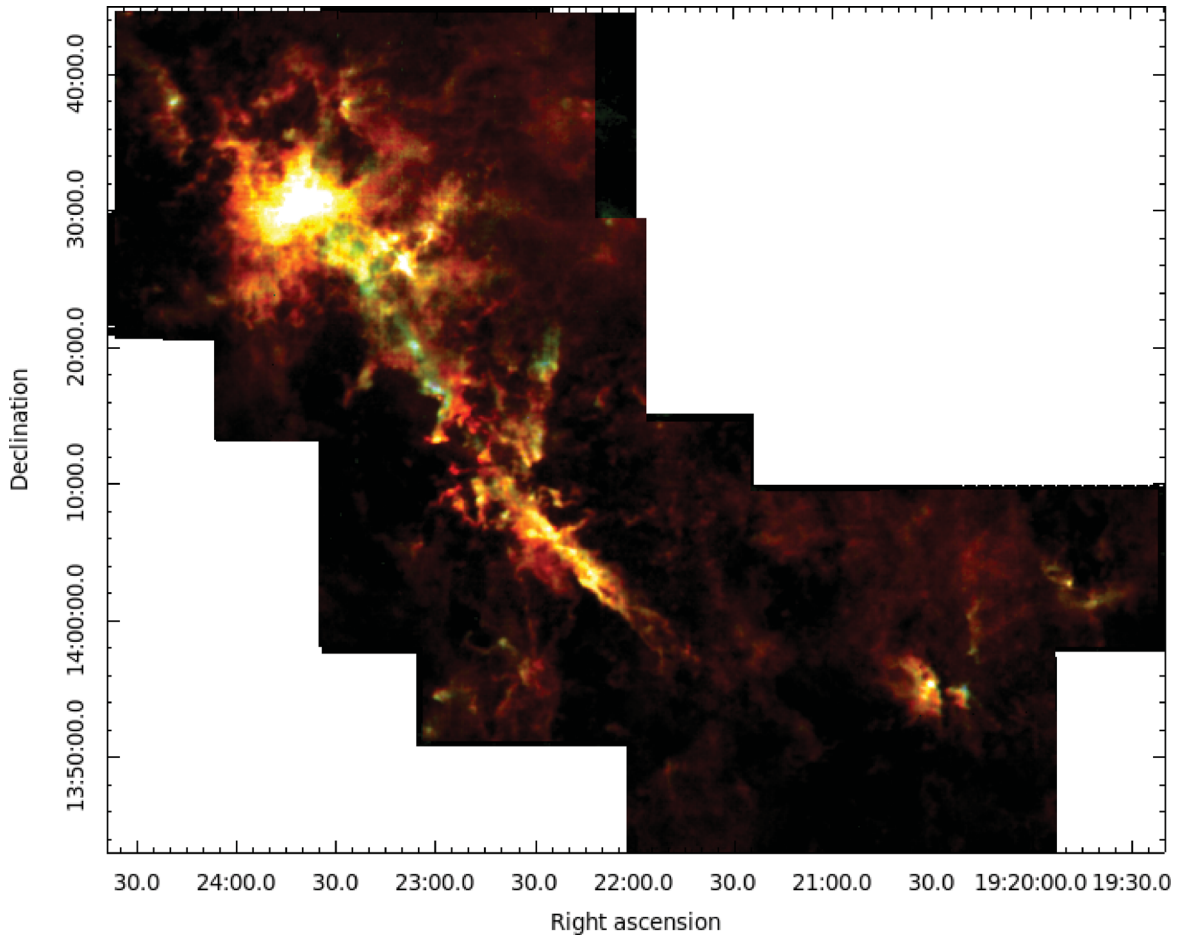


Figure 1. Three-colour integrated intensity image of the W51 GMC: ^{12}CO (red: scaled between 5 and 200 K km^{-1}), ^{13}CO (green: scaled between 5 and 75 K km^{-1}) and C^{18}O (blue: scaled between 5 and 25 K km^{-1}).

and cores. We define clumps as overdensities in a molecular cloud that may or may not contain cores from which single or multiple stars are born (also known as star-forming and ‘starless’ clumps, respectively; Williams, Blitz & McKee 2000).

To decompose the W51 GMC into clumps, we look to automated clump detection programs to deal with the large volume of data involved. Automated clump detection programs are beneficial as they are objective, repeatable and remove problems arising from classification by eye in complex areas and in particular where there is position–velocity data available. In this paper, we use the CUPID [part of the STARLINKproject software (see footnote 3)] clump-finding algorithm CLUMPFIND (Williams, de Geus & Blitz 1994). This algorithm was chosen in preference to other algorithms as no prior clump profile is assumed for each clump and it is a widely used algorithm (Moore et al. 2007; Buckle et al. 2010) which makes for better comparison between regions. CLUMPFIND works in a ‘top-down’ method by contouring the data and finding peaks within the data and then contouring down to a defined base level, detecting new peaks along the way and assigning pixels associated with more than one peak to a specific clump using the ‘friends-of-friends’ algorithm (Williams et al. 1994). Because of the intrinsic biases that are present in automated clump detection routines (Schneider & Brooks 2004; Smith, Clark & Bonnell 2008), we advise caution in blind cross-comparison of the properties of the clumps measured here with those from other clump detection algorithms, and we carefully

detail our chosen procedure to facilitate future cross-comparison with other data.

The CLUMPFIND algorithm was used on the S/N maps due to variations in rms estimates between maps as a result of changing opacity, elevation level and receiver performance. The output of this process produces a mask which can be applied to the integrated intensity maps to extract the intensities of the clumps.

In this work, we select a minimum contour level of 2σ (recall $\sigma = 0.4\text{ K}$) in order to obtain as much of the emission as possible without contamination from noise and use a contour spacing of 5σ so that the clumps are not broken up as much as they might be otherwise and to avoid artificial fragmentation. Clumps containing voxels touching the edge of the coverage area were excluded and a minimum clump size of 16 pixels was also specified. As we wish to only recover dense clumps and avoid regions of low surface brightness, we set a requirement of a 10σ detection at the peak, and clumps below this threshold are omitted from further analysis. If this cut is set to a lower value, we find that we recover more clumps that are larger with lower excitation temperatures. Clumps which have measured sizes that fall below the resolution of the data (i.e. $\Delta\text{RA} \leq 14\text{ arcsec}$ or $\Delta\text{Dec.} \leq 14\text{ arcsec}$ or $\Delta v \leq 0.5\text{ km s}^{-1}$) are also excluded to ensure the detection of real clumps only (following the method of Rathborne et al. 2009). We note that this criterion causes our catalogue to be incomplete for clumps with diameters less than $\sim 1\text{ pc}$ (this is the maximum diameter the smallest clump

can have whilst staying within the 16 pixels limit; see Section 3.2 for further details). We also set the criterion that a clump must be detected in *both* $^{13}\text{CO } J = 3-2$ and $\text{C}^{18}\text{O } J = 3-2$, to restrict our investigation to denser clumps, and set the requirement that the C^{18}O must have detections $>3\sigma$ at the peak. Other limits were investigated with 3σ chosen to retain more clumps within our sample, including more colder clumps than would have been otherwise included if a higher criterion such as 5σ was used. Finally, we exclude clumps with voxels touching the edge of the map area to avoid clumps where the full extent of the emission may not have been recovered.

3 RESULTS

3.1 Morphology

The complex clumpy nature of the W51 GMC is clearly seen in Fig. 1. Part of this complex nature is a result of projection effects from its situation at the tangential point of the Sagittarius arm where multiple clouds lie along the line of sight (Mufson & Liszt 1979). Classically, the W51 GMC has been discussed in terms of two main regions W51A and W51B, identified by their radio emission (Kundu & Velusamy 1967; Mufson & Liszt 1979; Kumar et al. 2004). More recently, this decomposition has been based on radial velocity data of the W51 GMC into the W51 complex and the high-velocity stream (HVS; Carpenter & Sanders 1998; Koo 1999; Okumura et al. 2000, 2001).

The position–velocity structure of the W51 GMC is shown in Fig. 2, and a histogram of clump velocities identified within this region, as discussed in Section 3.2, is given in Fig. 3. These figures show the complex nature of the W51 GMC with many components overlapping in radial velocity although the overall structure of the W51 complex, designated by Carpenter & Sanders (1998) as emission between 56 and 65 km s^{-1} , and the HVS as emission greater than 65 km s^{-1} , is visible. It should be noted that the small peak around 20 km s^{-1} is due to emission located at $19:20:31$ and $+13:55:23$ in RA and Dec. (seen in Fig. 1), which was not in the coverage area of the study by Carpenter & Sanders (1998), and hence not present within their data.

In the top image of Fig. 2, we see that the emission contributing to the W51A region originates from fragmented emission between 49 and 53 km s^{-1} . Carpenter & Sanders (1998) suggest that this emission is either a complex of individual clouds or remnants from larger clouds associated with H II region G49.4–0.3.

The middle image of Fig. 2 clearly shows W51A, roughly circular in shape with a size of approximately $30 \pm 10 \text{ pc}$ (at a distance of $6.5 \pm 1.5 \text{ kpc}$). Emission originating from the elongated structure, i.e. the HVS, is also detected in the bottom image of Fig. 2.

The HVS is delineated in velocity with a peak at $\sim 68 \text{ km s}^{-1}$ (Carpenter & Sanders 1998). Our data clearly show the HVS to be an elongated structure stretching roughly 1° in length and 5 arcmin in width running approximately parallel to the Galactic plane at $b \sim 3.5$. At a distance of 6.5 kpc, the HVS is estimated to extend approximately $100^{+40}_{-10} \text{ pc}$ in length and approximately 10 pc in width, giving rise to an aspect ratio >10 . Fig. 2 also shows pockets of higher integrated intensity visible throughout the entire length of the HVS at fairly regular intervals. Also visible are two notable breaks in the otherwise continuous structure of the HVS: one around RA $19:22:47$, Dec. $+14:12:47$ and the other around RA $19:24:10$, Dec. $+14:36:10$. From the images included in Fig. 2, we see that making clear distinctions between structures in velocity space is difficult as there are much overlap and complexity.

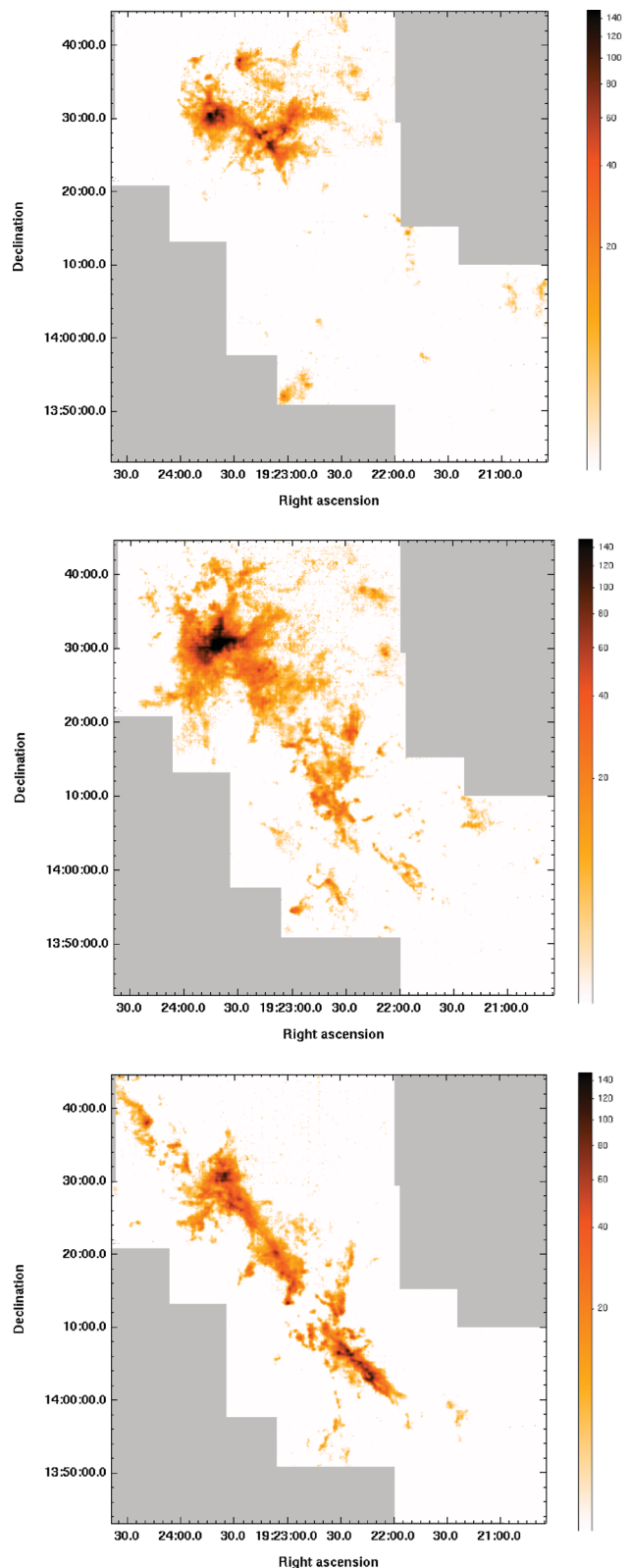


Figure 2. $^{13}\text{CO } (3-2)$ integrated intensity images of the W51 GMC (scaled logarithmically between 5 and 140 K km s^{-1}). Top: integrated between 45 and 55 km s^{-1} . Middle: integrated between 55 and 65 km s^{-1} , essentially the W51 complex. Bottom: integrated between 65 and 75 km s^{-1} , the HVS. Images exclude coverage on far right where emission is below 40 km s^{-1} .

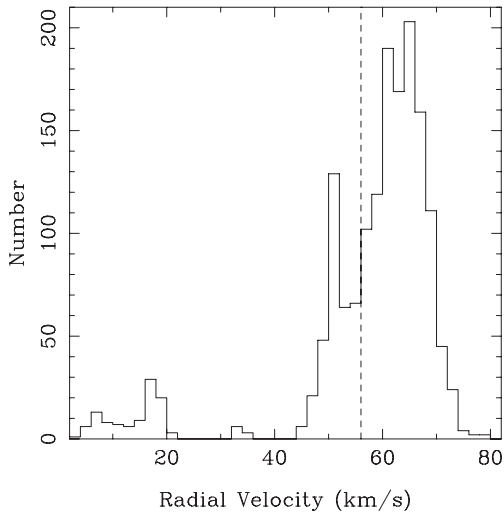


Figure 3. Histogram of clump radial velocities for the 1575 clumps identified by CLUMPFIND. The 56 km s^{-1} cut-off for the W51 GMC, as used by Carpenter & Sanders 1998, is marked by the dashed line.

Emission offset in position and velocity (between 5 and 35 km s^{-1}) from the W51 GMC was also detected by HARP within the mapped area. Carpenter & Sanders (1998) and Koo (1999) determined this emission to be nearby molecular clouds ($<2 \text{ kpc}$), which in Fig. 1 is the majority of the emission seen up to an RA of 19:21:00.0.

3.2 Clump catalogue

A total of 1575 clumps are identified within the region mapped by HARP. The output of the clump-finding algorithms are the position of the clump peak and clump centroid position in each of the three

axes, the size of the clump in each axis, total sum in the clump, peak value of the clump and the total number of pixels within the clump. The clump catalogue is given in Tables 1 and 2.

As the focus of this paper is to catalogue and obtain physical properties for those clumps associated with the W51 GMC, we first distinguish between those clumps associated with the W51 GMC and the foreground emission. Based on the discussion in Section 3.1, we designate those 445/1575 clumps with velocities less than 56 km s^{-1} as not associated with the W51 GMC. These clumps are given in Table 1 for completeness only but we do not examine them in further detail as they do not form part of this investigation. We decided to follow the convention of Carpenter & Sanders (1998) for the choice of velocity cut for ease of comparison, i.e. to the peak position of the ^{13}CO clumps. It is noted that this method of categorizing those clumps associated/not associated with the W51 GMC based on a simple velocity cut is an oversimplification (as seen in Figs 2 and 3); however, without a better understanding of the overlapping distributions of clump populations (in both position and velocity), there will undoubtedly be clumps incorrectly included or excluded from the sample. This same problem also occurs when assigning clumps identified to be associated with either the W51 complex or the HVS. Using central positions of the clumps or using positions as determined by the C^{18}O data as an alternative basis for clump classification does not affect the number of clumps by more than 2 per cent; it also does little to change the physical properties derived later in this paper.

Integrated intensity values were determined for the 1130 clumps with velocities greater than 56 km s^{-1} . We find average integrated intensity values for the 1130 clumps associated with the W51 GMC range between 1 and 103 K km s^{-1} with a median of 4 K km s^{-1} .

One-dimensional ^{13}CO velocity dispersions ($\sigma_{^{13}\text{CO}}$) were estimated by taking the size along the velocity axis as determined by CLUMPFIND (e.g. Buckle et al. 2010). These values range between 0.5 and 3.7 km s^{-1} with a median of 1.2 km s^{-1} and are shown in Fig. 4. The lower value to this range is set at the binned resolution

Table 1. Properties for the first 20 of 445/1575 clumps identified by CLUMPFIND within the region observed by HARP with velocities $<56 \text{ km s}^{-1}$. The full table is available as Supporting Information with the online version of the paper. Radial velocities (v_{rad}), linewidths (Δv), average integrated intensities (I_{av}), opacities (τ_{13}), diameters (D), excitation temperatures (T_{ex}), column densities [$N(\text{H}_2)$], mass estimates (M_{LTE}) and virial parameter (α) are given. Clump names are created from the l , b and v_{rad} positions of the individual clump centroid position.

Clump name	RA ($^{\circ}$)	Dec. ($^{\circ}$)	v_{rad} (km s^{-1})	Δv (km s^{-1})	I_{av} (K km s^{-1})	τ_{13}	D (pc)	T_{ex} (K)	$N(\text{H}_2)$ ($\times 10^{22} \text{ cm}^{-2}$)	M_{LTE} (M_{\odot})	α
G49.49−0.39+56.65	290.933	14.510	55.8	1.1	40.4	6.93	1.1	39.2	4.36	869	1.7
G49.49−0.39+52.21	290.933	14.508	53.3	2.0	24.1	4.29	1.2	38.3	1.63	409	0.2
G49.38−0.25+50.17	290.757	14.472	50.3	1.6	17.0	2.40	1.1	31.4	0.72	136	0.1
G48.61+0.03+17.48	290.129	13.923	18.3	2.3	15.1	2.40	0.9	31.2	0.64	99	0.1
G49.38−0.26+50.84	290.764	14.478	50.3	1.3	13.0	2.61	0.7	28.0	0.61	57	0.1
G49.37−0.30+50.15	290.791	14.443	51.3	2.1	18.2	4.87	1.7	28.5	1.48	722	0.3
G49.40−0.25+49.86	290.764	14.484	50.3	1.1	14.6	1.62	1.0	26.6	0.51	87	0.2
G49.48−0.39+54.10	290.933	14.506	54.3	1.2	35.6	3.30	1.0	37.6	1.90	332	0.6
G49.39−0.31+52.27	290.816	14.457	52.8	1.2	17.7	1.90	1.3	33.6	0.62	175	0.2
G49.49−0.37+47.72	290.916	14.512	48.8	1.1	12.7	2.13	1.0	29.3	0.51	93	0.2
G49.37−0.27+50.53	290.764	14.464	50.3	1.2	16.0	1.89	0.9	28.1	0.60	79	0.2
G49.39−0.25+49.13	290.753	14.482	49.3	1.4	14.7	2.69	0.9	22.5	0.81	111	0.2
G49.39−0.26+49.91	290.768	14.480	50.3	1.0	15.0	1.63	0.9	28.9	0.50	69	0.2
G49.49−0.37+50.94	290.918	14.514	50.3	1.2	28.3	2.72	0.9	28.4	1.37	181	0.4
G49.35−0.30+52.59	290.785	14.431	52.3	2.6	12.0	4.59	1.1	26.8	0.95	210	0.1
G49.36−0.30+51.69	290.787	14.439	51.8	1.9	18.7	3.25	1.0	28.3	1.05	173	0.1
G49.34−0.28+49.53	290.762	14.423	49.8	0.8	5.1	1.14	0.9	18.1	0.20	26	0.1
G49.48−0.39+49.75	290.933	14.496	50.3	1.1	8.1	4.08	1.4	21.9	0.65	206	0.3
G48.61+0.01+18.74	290.141	13.921	19.3	1.0	15.8	1.96	0.8	21.5	0.71	76	0.3
G49.40−0.30+54.34	290.801	14.468	55.3	1.5	17.9	1.34	1.0	26.8	0.55	100	0.1

Table 2. Properties for the first 20 of 1130/1575 clumps identified by CLUMPFIND associated with the W51 GMC. The full table is available as Supporting Information with the online version of the paper. Radial velocities (v_{rad}), linewidths (Δv), average integrated intensities (I_{av}), opacities (τ_{13}), diameters (D), excitation temperatures (T_{ex}), column densities [$N(\text{H}_2)$], mass estimates (M_{LTE}) and virial parameter (α) are given. Clump names are created from the l , b and v_{rad} positions of the individual clump centroid position.

Clump name	RA ($^{\circ}$)	Dec. ($^{\circ}$)	v_{rad} (km s^{-1})	Δv (km s^{-1})	I_{av} (K km s^{-1})	τ_{13}	D (pc)	T_{ex} (K)	$N(\text{H}_2)$ ($\times 10^{22} \text{ cm}^{-2}$)	M_{LTE} (M_{\odot})	α
G49.49−0.37+59.93	290.916	14.520	60.8	1.9	103.3	3.15	0.6	56.1	5.58	366	0.4
G49.49−0.37+57.72	290.924	14.514	59.3	1.6	38.6	1.76	0.9	37.9	1.28	185	0.2
G49.48−0.40+56.33	290.935	14.494	56.8	1.4	32.7	3.98	0.8	30.7	2.15	259	0.4
G49.48−0.40+57.52	290.935	14.496	57.8	1.0	35.2	2.01	0.8	36.0	1.28	123	0.4
G49.48−0.39+57.69	290.933	14.496	57.8	1.0	26.6	1.71	0.7	35.7	0.87	67	0.3
G49.50−0.38+59.94	290.929	14.518	60.3	1.4	42.7	3.95	0.8	38.8	2.68	293	0.5
G49.49−0.38+59.60	290.927	14.518	59.8	1.4	35.4	5.39	0.7	40.7	2.98	264	0.5
G49.00−0.32+72.48	290.628	14.110	72.8	1.6	8.9	1.78	1.1	27.4	0.32	70	0.1
G49.50−0.36+60.11	290.916	14.522	60.8	1.4	35.7	2.90	0.8	41.8	1.71	201	0.3
G49.49−0.38+58.96	290.929	14.508	58.3	1.0	41.4	5.21	0.6	37.6	3.39	188	0.8
G49.47−0.39+56.32	290.929	14.494	57.3	1.9	25.2	2.26	1.0	29.7	1.04	170	0.1
G49.01−0.30+67.02	290.616	14.122	67.8	1.6	12.8	1.14	0.8	26.4	0.37	36	0.1
G49.48−0.39+59.44	290.929	14.504	59.8	0.9	33.6	4.65	0.8	36.3	2.47	250	0.8
G49.48−0.37+62.57	290.916	14.514	62.3	1.5	40.0	5.25	0.7	31.6	3.39	260	0.5
G49.22−0.34+67.78	290.762	14.292	68.3	1.6	15.7	3.54	1.2	23.4	1.06	243	0.2
G49.18−0.35+68.77	290.745	14.255	68.8	1.2	11.7	1.05	0.9	26.5	0.32	46	0.1
G49.50−0.37+59.90	290.918	14.522	60.8	1.2	35.3	5.24	0.6	38.5	2.90	190	0.5
G49.47−0.38+63.77	290.918	14.504	63.3	1.5	32.8	3.42	1.1	37.2	1.81	388	0.4
G49.47−0.40+54.69	290.937	14.488	56.3	1.6	24.2	2.72	1.3	28.2	1.17	355	0.3
G49.50−0.38+61.93	290.929	14.528	62.8	1.4	26.9	6.34	0.9	30.1	2.78	419	0.6

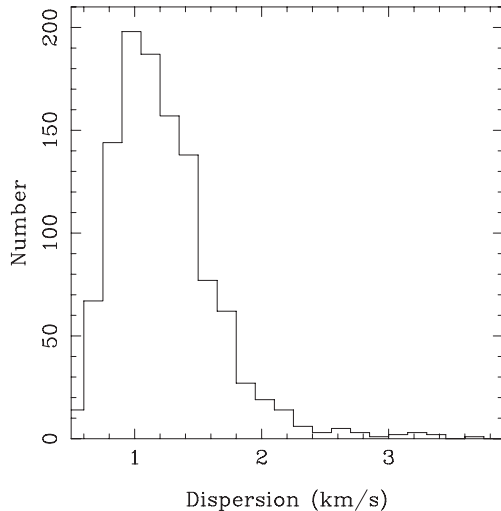


Figure 4. Histogram of clump dispersion linewidths for the 1130 clumps identified by CLUMPFIND (black line).

of the data, 0.5 km s^{-1} , which will be an upper estimate of the lower one-dimensional velocity dispersion.

Diameters of clumps used within this paper are the geometric averages of the diameters derived from the values reported by CLUMPFIND. The clump diameter reported by the algorithm is defined as the ‘rms deviation of each pixel centre from the clump centroid, where each pixel is weighted by the corresponding pixel data value⁵’, and as such we see that CLUMPFIND makes no assumption on the shape of a clump. We adopt a single distance of 6.5 kpc (see Section 3.4) and obtain diameters ranging between 0.5 and 3.4 pc with a median of 1.0 pc with errors dominated by the dis-

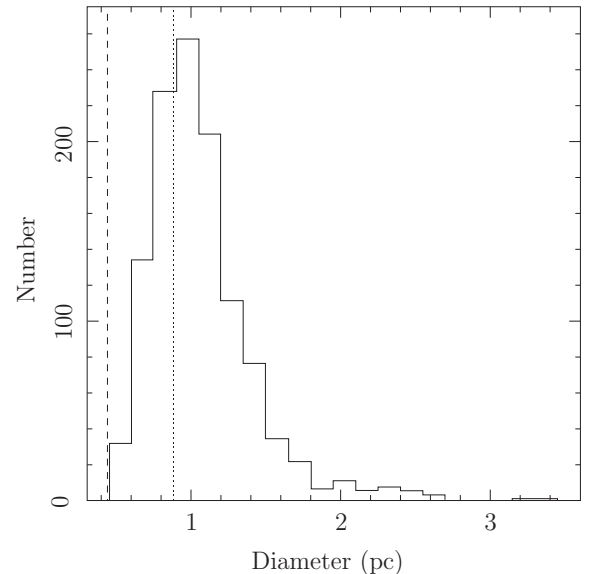


Figure 5. Histogram of clump diameters (pc) for the 1130 clumps identified by CLUMPFIND. The beam FWHM of the JCMT is indicated by the dashed line. The dotted line indicates the completeness of the catalogue based on detection requirements outlined in Section 2.3.

tance uncertainty ($6.5 \pm 1.5 \text{ kpc}$). A histogram of clump diameters is given in Fig. 5. This figure also depicts the completeness limit of the catalogue with a turnover at $\sim 1 \text{ pc}$. To the right of this turnover point, we note a significant number of clumps with diameters greater than 2 pc. The locations of these clumps (see Fig. 6) are typically in regions that are less populated, towards the edges of the complex. These clumps – with such large diameters – are likely to be clouds, rather than individual clumps, that have low surface brightnesses. These clouds likely have substructure within, but that substructure

⁵ See www.starlink.rl.ac.uk/star/docs/sun255.htx#xref_.

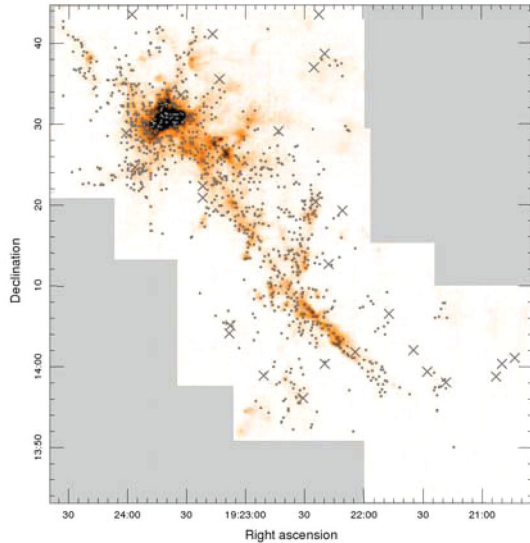


Figure 6. ^{13}CO (3–2) integrated intensity image of the W51 GMC region (scaled from 0 to 150 K km s^{-1}). Large crosses indicate the location of clumps with diameters above 2 pc, small crosses indicate the location of clumps with diameters less than this. Image excludes coverage on far right where emission is below 40 km s^{-1} as in Fig. 2.

being beneath the threshold of the clump-finding algorithm prevents distinctions between regions being made.

Systematic errors originating from the CLUMPFIND algorithm are non-trivial to quantify and so throughout this paper we report a representative error analysis and these are likely to be a lower limit to the true uncertainty.

3.3 Opacities

We obtain opacities based on ratios between the peak receiver temperatures for ^{13}CO [$T_R(^{13}\text{CO})$] and C^{18}O [$T_R(\text{C}^{18}\text{O})$], assuming that the excitation temperature, T_{ex} , beam filling factor and telescope beam efficiency remain constant for a particular observed source (e.g. Myers, Linke & Benson 1983; Ladd, Fuller & Deane 1998; Buckle et al. 2010; Curtis, Richer & Buckle 2010). The ratio R_{1318} is given by

$$R_{1318} = \frac{T_R(^{13}\text{CO})}{T_R(\text{C}^{18}\text{O})} \approx \frac{1 - e^{-\tau_{13}}}{1 - e^{-\tau_{18}}} \approx \frac{1 - e^{-\tau_{13}}}{1 - e^{-\tau_{13}/X}}, \quad (1)$$

where τ_{13} and τ_{18} are the optical depths of ^{13}CO and C^{18}O , respectively, and X is the abundance ratio of ^{13}CO relative to C^{18}O molecules. If the lines are optically thin, then this ratio R_{1318} tends to the abundance ratio, X , of the molecules. Estimating abundance ratios is non-trivial and can vary across a range of environments across the Galaxy (Wilson & Rood 1994) and within regions, e.g. within photon-dominated regions (Störzer et al. 2000).

To estimate X , we inspected the variation of R_{1318} across the region observed by HARP (shown in Fig. 7). Obtaining a good estimate of R_{1318} across the region requires the extent of the emission along the radial velocity axis to be the same for both isotopologues, i.e. they have the same gas. In order to ensure this, we applied a 5σ cut to the C^{18}O data and used this as a mask to extract the ^{13}CO data. From Fig. 7, we find $R_{1318} \sim 6$ –8, but decreasing to 2 towards the more dense regions. This decrease to lower values is likely due to the ^{13}CO being optically thick at the filament cores rather than due to changes in abundance (e.g. freeze out). As we can only make the assumption that R_{1318} tends to X in optically thin regions, we use

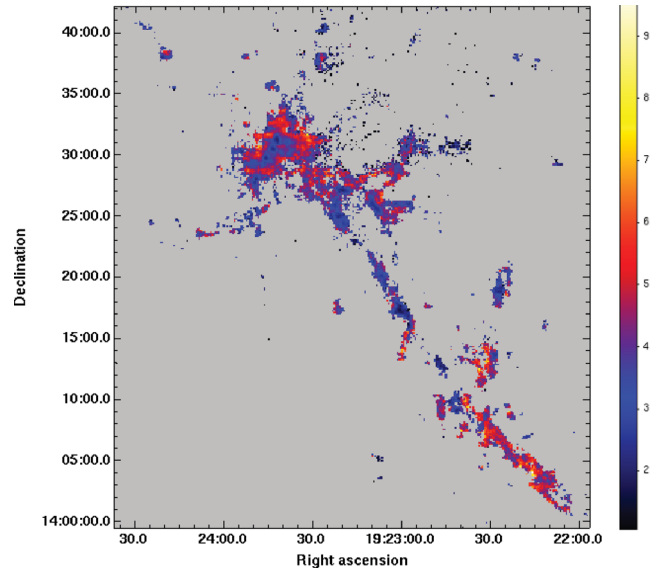


Figure 7. Ratio of ^{13}CO to C^{18}O for the W51 GMC. This image does not cover the entire region observed but shows the main regions of interest. Pixels are displayed if peak intensities $> 5\sigma$.

the values obtained in the less dense regions, resulting in a value of $X[^{13}\text{CO}/\text{C}^{18}\text{O}] = 7 \pm 1$.

The decrease in R_{1318} we see is consistent with observations by Curtis et al. (2010), who report $R_{1318} \sim 7$ at edges of the emission regions and 2–4 towards the centre of the denser regions. Buckle et al. (2010), investigating Orion B, find the ratio tending to 10 ± 2 at the edge of the C^{18}O emission in NGC 2024 and 7.5 ± 1.5 in NGC 2071. Both regions have ratios tending to ~ 2 in the denser parts. Our estimate of $X[^{13}\text{CO}/\text{C}^{18}\text{O}] = 7 \pm 1$ is consistent with these observations. By assuming that this abundance holds for the whole of the W51 GMC, τ_{13} may be calculated for all clumps.

For the 1130 clumps examined, we find that the clumps are found to be predominantly optically thick, with values of τ_{13} up to 11.9 with a median of 2.6 and with 94 per cent of the clumps having $\tau_{13} \geq 1$. The main source of error in determining optical depths is the determination of $X[^{13}\text{CO}/\text{C}^{18}\text{O}]$ for the W51 GMC which we take to be 7 ± 1 . By decreasing $X[^{13}\text{CO}/\text{C}^{18}\text{O}]$ to 6, we find the number of clumps that are optically thick decreases to 85 per cent with a median $\tau_{13} = 2.0$, whilst increasing $X[^{13}\text{CO}/\text{C}^{18}\text{O}]$ to 8 takes the number of optically thick clumps up to 98 per cent with a median $\tau_{13} = 3.0$. A further source of uncertainty originates from the fact that as the observed R_{1318} tends to X in equation (1), τ_{13} tends to zero, so smaller values of τ_{13} have greater associated uncertainties.

3.4 Distance to W51

The determination of the distance to the W51 GMC remains non-trivial, predominantly due to the location of the complex at the tangent point of the Sagittarius arm. From the literature, we find a range of heliocentric distance estimates to the W51 GMC, which we discuss in detail below.

Based on 21 cm absorption features, Sato (1973) determined the distance to two H II regions in W51A to be located at a distance of 8 kpc. Carpenter & Sanders (1998) used a proper motion study of masers within G49.5–0.4 to derive a similar distance of $7.0 \pm 1.5 \text{ kpc}$. Some parts of W51A have been found to lie at a different distance, possibly as a result of projection effects from clouds at differing distances. Sato et al. (2010) using 22 GHz

H₂O masers obtained parallax distance of $5.41^{+0.31}_{-0.28}$ kpc to W51. Russeil (2003) reports a distance to W51A of 5.5 kpc. W51 IRS 2 has been found to lie at a distance of $5.1^{+2.9}_{-1.4}$ kpc (Xu et al. 2009). Sato (1973) also determined distances to H II regions in W51B based on 21 cm absorption and found them located at a distance ~ 6.5 kpc. Koo (1999) also reported a distance between 6.4 and 6.9 kpc based on kinematic CO observations.

A significantly smaller distance has also been determined to newly formed OB stars associated with W51A. Figuerêdo et al. (2008) determined a distance to W51A of 2.0 ± 0.3 kpc using spectroscopic parallaxes. However, as discussed in Clark et al. (2009), the reason for an underestimation in this distance estimate is likely to be a result of the adoption of an incorrect reddening law, multiplicity or incorrect spectral classification. As a result, we decide to adopt a single distance estimate of 6.5 ± 1.5 kpc.

3.5 Temperature

To obtain the excitation temperature of the clumps, we make three assumptions: first, that the clumps are in local thermodynamic equilibrium (LTE); secondly, that the emission line used in this determination is optically thick (as found in Section 3.3) and, thirdly, that the emission fills the beam (see Fig. 5). We calculate excitation temperatures using ¹³CO in preference to ¹²CO because ¹²CO is likely to be self-absorbed within such a dense and complex environment. With these assumptions, we use

$$T_{\text{ex}} = \frac{T_0}{\ln \left[1 + \frac{T_0}{T_{\text{max}} + T_0 / (e^{T_0/T_{\text{bg}}} - 1)} \right]}, \quad (2)$$

where $T_0 = h\nu/k$, h is the Planck constant, k is the Boltzmann constant, T_{max} is the antenna temperature at the peak of the clump and T_{bg} is the 2.7 K cosmic microwave background radiation. For ¹³CO $J = 3-2$, this equation becomes

$$T_{\text{ex}} = \frac{15.9 \text{ K}}{\ln [1 + 15.9 \text{ K} / (T_{\text{R}} + 0.045 \text{ K})]}. \quad (3)$$

Excitation temperatures were derived for the 1130 clumps in our catalogue and range between 7 and 56 K with a median temperature of 12 K. Temperatures derived here are lower estimates for T_{ex} as they may be affected by any line asymmetries present and beam dilution.

3.6 Densities

Once temperatures have been determined, it is possible to calculate values for column densities for ¹³CO, correcting for optical depth effects by using the opacities calculated in Section 3.3, using the following equation (see e.g. Garden et al. 1991):

$$N_{\text{tot}} = \frac{3k}{8\pi^3 B Z^2} \frac{e^{hBJ(J+1)/kT_{\text{ex}}}}{(J+1)} \frac{(T_{\text{ex}} + hB/3k)}{1 - e^{-h\nu/kT_{\text{ex}}}} \int \tau_{\nu} d\nu, \quad (4)$$

where Z is the partition function in cgs units, B is the rotation constant of the molecule in MHz, J is the upper level of the transition and ν is measured in km s⁻¹. The relation (from equation 14.55 in Rohlfs & Wilson 2004)

$$T_{\text{ex}} \int \tau_{\nu} d\nu = \frac{\tau_0}{1 - e^{-\tau_0}} \int T_{\text{mb}} d\nu, \quad (5)$$

where $\int T_{\text{mb}} d\nu$ is essentially the integrated intensity of the line (K km s⁻¹). Combining and evaluating the previous two equations yields column densities in terms of cm⁻². For ¹³CO (3-2), with $\nu =$

330.588 GHz, $B = 55\,101.011$ MHz and $Z = 0.11 \times 10^{-18}$ esu cm, we see

$$N_{\text{13CO}} = \frac{(2.26 \times 10^{13})(e^{31.72/T_{\text{ex}}})(T_{\text{ex}} + 0.88)}{1 - e^{-15.87/T_{\text{ex}}}} \frac{1}{T_{\text{ex}}} \times \left(\frac{\tau_0}{1 - e^{-\tau_0}} \right) \int T_{\text{mb}} d\nu \text{ cm}^{-2}. \quad (6)$$

Column densities in terms of H₂ as opposed to ¹³CO are determined using the abundance ratio $[^{13}\text{CO}]/[\text{H}_2] \sim 10^{-6}$, which is based on $[^{12}\text{CO}]/[\text{H}_2] \sim 10^{-4}$ and $[^{13}\text{CO}]/[^{12}\text{CO}] \sim 10^{-2}$ (Wilson, Langer & Goldsmith 1981; Frerking, Langer & Wilson 1982; Wilson 1999).

The range of N_{H_2} values that we determine are between $7.4 \pm 1.2 \times 10^{20}$ and $5.6^{+0.8}_{-0.9} \times 10^{22}$ cm⁻², with a median $5.6 \pm 0.8 \times 10^{21}$ cm⁻² and with errors originating from uncertainties in opacities and the abundance ratio.

Surface densities, with units g cm⁻², are calculated by multiplying the column density by the mass of molecular hydrogen. Within the W51 GMC, we find surface densities ranging between 0.002 and 0.19 g cm⁻² with a median of 0.02 g cm⁻². Systematic errors in the surface density derived here may arise from both the abundance ratio and distance, the combination of which may change the range in derived surface densities to 0.002–0.21 g cm⁻² with median values of the order of 0.02 g cm⁻².

3.7 Mass

Once the density and size of a clump have been determined, it is possible to calculate the mass of the clump via

$$M_{\text{LTE}} = A N_{\text{13CO}} \frac{[\text{H}_2]}{[^{13}\text{CO}]} \mu_{\text{H}_2} m_{\text{H}}, \quad (7)$$

where A is the area of the clump, N_{13CO} is the source-averaged column density, the abundance ratio is again assumed to be $[\text{H}_2]/[^{13}\text{CO}] \sim 10^6$, μ_{H_2} is the mean molecular weight of the gas per H₂ molecule ($\mu_{\text{H}_2} = 2.72$ to include hydrogen, helium and the isotopologues of carbon monoxide; e.g. Buckle et al. 2010) and m_{H} is the mass of hydrogen.

Our clump mass estimates, based on the assumption of LTE, range between 10 and 1700 M_⊙ with a median of 90 M_⊙ (see Fig. 8). Sources of error in mass come from distance estimates and also the abundance ratio. This means that the masses of the clumps may lie anywhere within the range 10–860 M_⊙ with a median of 50 M_⊙ (taking a distance of 5 kpc and an $X[^{13}\text{CO}/\text{C}^{18}\text{O}]$ of 6) or 10–2950 M_⊙ with a median of 160 M_⊙ (taking a distance of 8 kpc and an $X[^{13}\text{CO}/\text{C}^{18}\text{O}]$ of 8). These estimates may also be lower limits due to the depletion of CO on to the dust at low temperatures and high densities with dust mass estimates needed to investigate how much this will affect these values for the complex.

Summing the masses determined for individual clumps from equation (7), we find a total mass for dense material of 1.5×10^5 M_⊙ for the entire W51 GMC (including W51 complex and the HVS). Again, variations in distance estimates and abundance ratios mean this value may vary between 7.7×10^4 and 2.7×10^5 M_⊙.

3.8 Clump criticality

To determine if the clumps are subcritical or supercritical, we compare linewidths observed to those predicted to be produced from thermal processes alone using

$$\Delta v_{\text{FWHM}} = \left[\frac{8 \ln(2) k T_{\text{ex}}}{m_{\text{13CO}}} \right]^{1/2}, \quad (8)$$

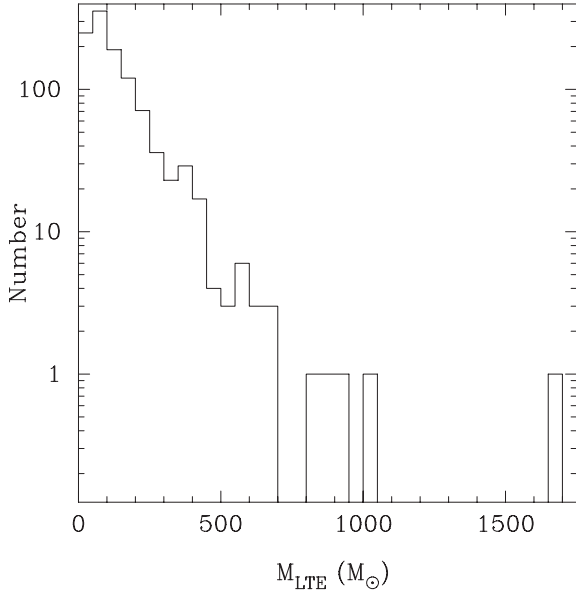


Figure 8. Histogram of clump masses (M_{\odot}) for the 1130 clumps identified by CLUMPFIND (black line).

where Δv_{FWHM} is the expected linewidth produced by thermal processes, and $m_{^{13}\text{CO}}$ is the molecular mass of ^{13}CO . These expected values range between 0.1 and 0.3 km s^{-1} ; however, as seen in Section 3.2 our binned data will not show structures less than 0.5 km s^{-1} . An inspection of the integrated weighted velocity dispersion over the W51 GMC region at a 0.1 km s^{-1} resolution reveals the majority of the dispersion to be $>0.5 \text{ km s}^{-1}$ (see Fig. 9). What we do see in Fig. 4 is a turnover at $\sim 1.0 \text{ km s}^{-1}$, which along with the above evidence implies that we are close to complete in our dispersion estimates, indicating that all the clumps have lines that are super thermal, indicating that turbulence may dominate within these clumps. To determine if the clumps are subcritical or supercritical, we determine the virial mass, M_V , of each clump:

$$M_V = R \sigma_{v,3D}^2 / G, \quad (9)$$

which assumes a clump density profile of $\rho \propto r^{-2}$ (MacLaren, Richardson & Wolfendale 1988; Williams et al. 1994). In the equa-

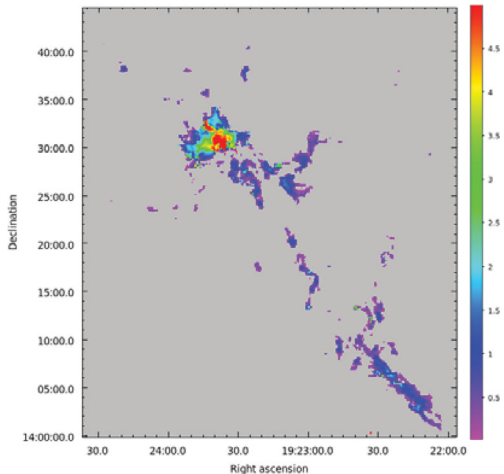


Figure 9. Integrated weighted velocity dispersion, from 0 to 5 km s^{-1} , for ^{13}CO emission taken from data with resolution of 0.1 km s^{-1} . Pixels are displayed if they have emission $>10 \sigma$.

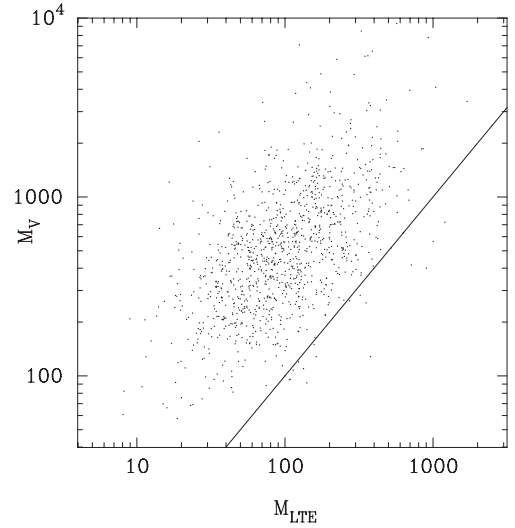


Figure 10. Plot of virial mass (M_V) to clump mass (M_{LTE}) for the 1130 clumps identified by CLUMPFIND. Clumps with a ratio $M_{\text{LTE}}/M_V \geq 1$ are supercritical and likely to collapse. The line of equality for M_{LTE} and M_V is plotted so we see clumps that lie above and to the left of this line, the majority of the clumps in our sample, are subcritical. We find 1 per cent of the clumps by number are supercritical.

tion, R is the clump radius, G is the gravitational constant and $\sigma_{v,3D}^2$ is the three-dimensional velocity dispersion as given by

$$\Delta v^2 = \sigma_{v,3D}^2 = 3 \left[\sigma_{^{13}\text{CO}}^2 + \frac{kT}{m_H} \left(\frac{1}{\mu} - \frac{1}{m_{^{13}\text{CO}}} \right) \right], \quad (10)$$

where $\sigma_{^{13}\text{CO}}^2$ is the one-dimensional velocity dispersion of ^{13}CO (see Section 3.2), k is the Boltzmann's constant, T is the kinetic temperature of the gas which we assume to equal the excitation temperature (e.g. Buckle et al. 2010).

Errors in M_V originate from errors in both size (originating in distance) and linewidths, both of which are obtained using CLUMPFIND and as stated in Section 3.2 are not easily quantified. To get a handle on the errors, we estimate these to be as stated in Section 3.2 for R and of the order of 0.25 in velocity dispersion ($\sigma_{^{13}\text{CO}}^2$), half the binned spectral resolution. A clump is likely to collapse if it is supercritical with a virial parameter, $M_{\text{LTE}}/M_V > 1$. Of the 1130 clumps associated with the W51 GMC, we find they span a range of virial parameters 0.01–2.8 with a median of 0.2 with 1 per cent of the clumps by number (14/1130) and 4 per cent by mass found to be supercritical. A plot of the distribution of virial mass versus clump mass is given in Fig. 10.

Errors associated with determining the virial parameter [full width at half-maximum (FWHM), distance and abundance ratio] result in a range of 0.1–22 per cent of clumps, by number, being supercritical. Errors also arise from the assumption of a spherical geometry.

4 DISCUSSION

In our study, we have located 1130 clumps associated with the W51 GMC using the CLUMPFIND algorithm. We find these clumps have characteristic diameters of 1.0 pc (0.5–3.4 pc), excitation temperatures of 12 K (7–56 K), densities of $5.6 \times 10^{21} \text{ cm}^{-2}$ (7.4×10^{20} to $5.6 \times 10^{22} \text{ cm}^{-2}$) and masses of 90 M_{\odot} (10–1700 M_{\odot}), with 1 per cent of clumps by number (4 per cent by mass) found to be supercritical. With a total mass (including all clumps with radial velocities $>56 \text{ km s}^{-1}$) of $1.5 \times 10^5 M_{\odot}$, this places the W51 GMC

in the top end (5–10 per cent) of GMCs in terms of mass (e.g. Solomon et al. 1987; Carpenter & Sanders 1998; Hindson et al. 2010).

In this section, we focus first on the global properties of the W51 GMC, such as the amount of dense material contained within the W51 complex and HVS, the clump-forming efficiency (CFE) of the region and the distribution of clump masses. Finally, we combine what we know about the properties of the complex and of the individual clumps to yield an insight into the incipient star formation potential of the W51 GMC.

4.1 Clump-forming efficiencies

Star formation has been found to be an inefficient process; on the Galactic level the SFE is observed to be ~ 2 per cent (Myers et al. 1986). This inefficiency is due to either of two reasons: it is an inherently inefficient process or it is a slow process and so appears to be inefficient (Bonnell et al. 2011). From the observations presented in this paper (see Section 3.7), we find that the entire W51 GMC has a total dense molecular reservoir for star formation of the order of $1.5 \times 10^5 M_\odot$. These dense clumps formed from the diffuse molecular material traced by Carpenter & Sanders (1998), in ^{12}CO (1–0). We may therefore obtain a dense CFE for the complex by comparing our mass estimates of the individual clumps (M_{dense}) with the mass estimate from the diffuse material (M_{diffuse}) over the entire region as observed by Carpenter & Sanders (1998). We obtain the CFE using

$$\text{CFE} = \left(\frac{M_{\text{dense}}}{M_{\text{dense}} + M_{\text{diffuse}}} \right). \quad (11)$$

For a direct comparison, we only include clumps with velocities between 56 and 71 km s $^{-1}$ (56–65 km s $^{-1}$ for the W51 complex and 65–71 km s $^{-1}$ for the HVS as defined by Carpenter & Sanders 1998; see Table 3). We find for the complex as a whole a CFE of 14 ± 1 per cent with a lower (11 ± 1 per cent) and a higher (29 ± 2 per cent) value for the W51 complex and HVS, respectively (see Table 3). Errors on this CFE originate from both the M_{LTE} and M_{V} estimates derived within this paper, as outlined in Section 3.7, and from the masses reported by Carpenter & Sanders (1998) although the authors do not indicate the reliability of these values and so are not included in these representative errors. An additional source of error originates in the assumption that the ^{12}CO (1–0) traces both the diffuse material and the same dense material as traced by the ^{13}CO (3–2) emission.

From the CFE values derived, we find the following results. First, we established that the CFE within the entire complex is much higher than the galactic SFE and is higher than SFEs previously reported for the W51 GMC (2–8 per cent; Okumura et al. 2000). This seems to be well established with similar CFE values for other

GMCs; e.g. the CFEs of NGC 2024 and 2071, two regions within the Orion B complex, have a reported CFE of 33 and 24 per cent, respectively, based on the mass ratio of ^{12}CO to ^{13}CO (Buckle et al. 2010).

The second result we find is an increase in efficiency between the HVS (29 ± 2 per cent) compared to the W51 complex (11 ± 1 per cent). Differences in CFEs have been observed across other complexes, i.e. W3 has a CFE for dense clumps of 26 per cent in the high-density layer and only 5 per cent in the diffuse cloud (Moore et al. 2007). Moore et al. (2007) conclude that the formation of dense clumps is more efficient when it has been shocked by external interactions.

These CFE values only go so far in unlocking the picture of star formation as not all clumps necessarily go on to form stars. We saw in Section 3.7 that 1 per cent of the clumps by number (4 per cent by mass) within the complex are supercritical ($M_{\text{LTE}}/M_{\text{V}} > 1$) and have the potential to form stars in the future. It is therefore more informative to report the supercritical clump-forming efficiency (SCFE), as this is more likely to reflect a truer picture of how the star formation efficiency will evolve over future generations. We estimate the SCFE using

$$\text{SCFE} = \left(\frac{M_{\text{sup}}}{M_{\text{dense}} + M_{\text{diffuse}}} \right), \quad (12)$$

where M_{sup} is the mass of supercritical clumps. We find an SCFE for the W51 GMC of $0.5^{+2.3}_{-0.3}$ per cent, W51 complex of $0.6^{+2.6}_{-0.5}$ per cent and $0.1^{+3.5}_{-0.1}$ per cent for the HVS (as given in Table 3). Errors here are similar to before but are also affected by errors in distance, abundance ratio and the FWHM of the clumps.

This leads us to our third result that the SCFEs obtained are below the SFE reported for the W51 GMC (2–8 per cent; Okumura et al. 2000). This result is dependant on several factors: (i) the fractional mass within the supercritical clumps that will go on to the final star (which would decrease this estimate), (ii) the number of subcritical clumps containing supercritical cores within them (which would increase this estimate) and (iii) the formation of future cores from the diffuse gas. Placing a quantitative value on these other factors is non-trivial as it must account for possible fragmentation, resolution limitations with the current data and other factors such as the mode of massive star formation (see McKee & Ostriker 2007). If we consider this SCFE for the whole complex of $0.5^{+2.3}_{-0.5}$ per cent independently, it would indicate that star formation will likely diminish over time unless some future triggering event occurs. Considering the SCFE may not tell the entire story of the future of star formation within W51. Buckle et al. (2010), studying condensations within the Orion B complex, also find the majority of clumps to contain $M_{\text{V}} > M_{\text{LTE}}$. Buckle et al. (2010) cite large uncertainties in distance estimates, fractional abundances, excitation temperatures and assumed density profile, which result in the inability to make definitive conclusions about any particular condensation. Additionally, evidence based on molecular outflows detected in the ^{12}CO data indicates that star formation within this region is ongoing. This outflow work will be presented in a subsequent paper.

Another way to consider the future of star formation within the W51 complex is by comparing the surface densities observed within the GMC to those observed within massive star-forming regions. Observational studies such as Plume et al. (1997) and those outlined in McKee & Tan (2003) and McKee & Ostriker (2007) find that massive stars have only been observed in regions with surface densities greater than $\sim 1.0 \text{ g cm}^{-2}$ and only low-mass stars form when surface densities are around $\sim 0.03 \text{ g cm}^{-2}$ or lower, with theoretical justification provided by Krumholz & McKee (2008).

Table 3. Physical properties for clumps within the velocity range (56–71 km s $^{-1}$) as used by Carpenter & Sanders (1998). M_{LTE} estimates are from this paper and diffuse mass estimates M_{XCO} come from Carpenter & Sanders (1998) recalculated to a distance of 6.5 kpc. Other properties reported are the clump-forming efficiency (CFE) and the supercritical clump-forming efficiency (SCFE).

Region	M_{LTE} ($\times 10^5 M_\odot$)	M_{XCO} ($\times 10^5 M_\odot$)	CFE (per cent)	SCFE (per cent)
W51 GMC	1.5	11	14	0.5
W51 complex	1.0	9.5	11	0.6
HVS	0.4	1.5	29	0.1

Surface densities, derived within Section 3.6, range between 0.002 and 0.19 g cm^{-2} (median of 0.02 g cm^{-2}). These surface densities are lower than expected for sites of massive star formation but are consistent with observations by Elia et al. (2010) and Roy et al. (2011), who find values down to 0.001 g cm^{-2} . Elia et al. (2010) derived values $< 1 \text{ g cm}^{-2}$ from two regions within the Herschel Infrared GALactic Plane Survey (Hi-GAL) key-project data (Molinari et al. 2010a). Roy et al. (2011) found a similar result based on *Balloon-borne Large Aperture Submillimeter Telescope* (BLAST; Pascale et al. 2008) observations of the Cygnus-X star-forming region. A likely explanation for these low surface density values was proposed by Roy et al. (2011), who suggested that these values may evolve to higher surface densities over time, with the cold precursors of dense clusters having massive reservoirs yet to be channelled by gravity into a higher surface density state and so being more extended objects than clumps.

Finally, we compare our clump masses for the W51 GMC with masses of clusters within the W51 GMC based on the study by Kumar et al. (2004). Kumar et al. (2004) derive total cluster mass for the region of $3 \times 10^4 M_{\odot}$. We obtain a cluster formation efficiency (CLFE) by comparing this total cluster mass (M_{cluster}) with the aggregate dense molecular mass of the W51 GMC:

$$\text{CLFE} = \left(\frac{M_{\text{cluster}}}{M_{\text{cluster}} + M_{\text{dense}}} \right). \quad (13)$$

This leads us to a value of 16_{-6}^{+12} per cent.

4.2 The clump mass distribution

The clump mass distribution (CMD) describes the relative frequency of clumps with differing masses, which is commonly fitted by a basic power law

$$\frac{dN}{dM} \propto M^{-\alpha}. \quad (14)$$

The shape of the CMD has been seen to resemble the stellar initial mass function (IMF) that describes the relative frequency of stars with differing masses (e.g. Salpeter 1955; Kroupa 2001) over a range of environments (Kramer et al. 1998; Motte, Andre & Neri 1998; Nutter & Ward-Thompson 2007; Simpson, Nutter & Ward-Thompson 2008). For example, observations of Orion find single power-law fits to a CMD of 1.3 and 1.7 for NGC 2024 and 2071, respectively, and 2.3 and 2.6 for the upper end of a double power law characterizing the CMD (Buckle et al. 2010). Observations of dense clumps within W3 by Moore et al. (2007) also find values between 1.5 and 1.66 for CMDs obtained using a single power law and 1.8 and 1.85 for the higher mass end (above what they call the log 1.8 mass structure; see Moore et al. 2007, for further details).

Understanding the relationship between the CMD and the IMF can help constrain star formation models (Bate & Bonnell 2005; Reid & Wilson 2006a) although the full physical meaning remains unclear due to a number of complications: (i) differing forms of the distribution, (ii) completeness limitations, (iii) nature of the objects, (iv) multiplicity, (v) efficiency, (vi) time-scales, (vii) physical size scales, (viii) telescope resolution and (ix) distance, as discussed by Curtis & Richer (2010) and Reid et al. (2010). Nevertheless, it is instructive to compare the CMD of the W51 GMC with other nearby regions in order to investigate differences caused by distance.

We used a differential form of the CMD as it allows for a more straightforward accounting of uncertainties (see Fig. 11). To minimize Poisson uncertainties caused by fixed bin widths, we follow the method of Maíz Apellániz & Úbeda (2005) using a variable

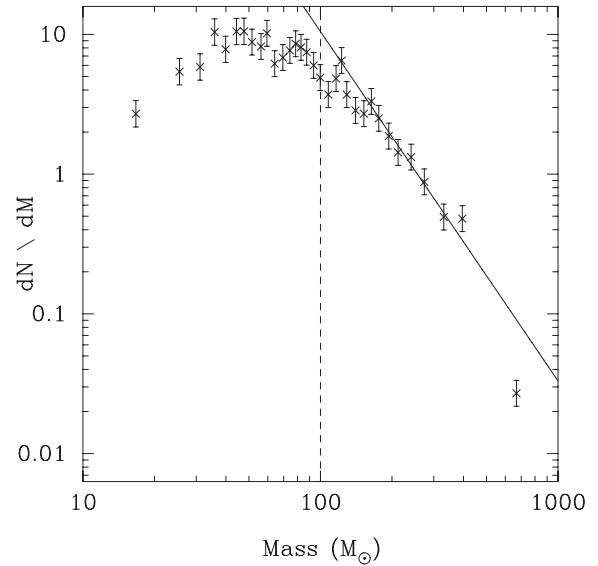


Figure 11. Differential CMD of the W51 GMC, with the sample average completeness limit, M_{limit} , of the clumps indicated by a vertical dashed line. The data are fitted with a single power law for masses $M_{\text{LTE}} > M_{\text{limit}}$. We find that the CMD is best described by $\alpha = 2.4_{-0.1}^{+0.2}$.

bin width with a fixed number of clumps per bin (e.g. Reid & Wilson 2006b). When fitting to our data, we do not want to include points below the completeness level of our data. We follow Curtis et al. (2010) and calculate the ‘sample average completeness limit’, M_{limit} , which is the mass of an average-sized clump at the 10σ detection threshold. We take the median clump size, velocity dispersion and opacity from clumps with higher σ limits to ensure the median values we do use are unaffected by incompleteness. From this, we calculate $M_{\text{limit}} = 100 M_{\odot}$.

We use χ^2 fitting technique to fit a single power law to our CMD for clumps with masses $M_{\text{LTE}} > M_{\text{limit}}$. We find that the W51 GMC is best described by $\alpha = 2.4_{-0.1}^{+0.2}$, with $\chi^2_{\text{red}} = 4.0$ [where $\chi^2_{\text{red}} = \chi^2 / (k - N)$ for k bins and N parameters, with an ideal χ^2_{red} between 1 and 2, indicating a good fit to the data]. We also find that both the W51 complex and the HVS are best described by this same single power law ($\alpha = -2.4$) within the errors.

Our value of $\alpha = 2.4_{-0.1}^{+0.2}$ is higher than other single power-law fits to other regions, but it is in agreement to the upper mass end of two-component power-law fits reported in the literature (e.g. Moore et al. 2007; Buckle et al. 2010). This is unsurprising as due to completeness we only fit to the upper mass end of our CMD, with masses of the order of 10^2 – $10^3 M_{\odot}$. At these high masses, it is worth noting that with a tentative upper mass limit to the IMF of $\sim 300 M_{\odot}$ (Crowther et al. 2010) these are the clumps most likely to form hierarchical multiple systems, i.e. binaries or stellar clusters. We refrain from comparing this higher mass end of our CMD to any cluster mass function because, as with the IMF, there are many pitfalls in a direct comparison including changes over time caused by gas expulsion, the loss of stars and the destruction of the clusters itself (Parmentier et al. 2009).

Previous studies of the W51 GMC have investigated the form of the mass distribution (or function): Okumura et al. (2000) looked at the IMF for central part of the W51 GMC and found $\alpha = 2.8$, and Kang et al. (2009) looked at the mass function for young stellar objects associated with the active region of the W51 GMC and observed $\alpha = 2.26$. Our single power-law fit with $\alpha = -2.4_{-0.1}^{+0.2}$ is

in agreement with those later mass functions observed within the W51 GMC and the Salpeter IMF.

4.3 Location of the supercritical clumps

To look at how star formation is spatially developing in the W51 GMC, we use the location of the supercritical clumps to indicate where the future of star formation is likely to occur. We also use young clusters, as catalogued by Bica et al. (2003) and Kumar et al. (2004), to place past star formation activity. The catalogue by Bica et al. (2003) presented new observations and previous results by Goldader & Wynn-Williams (1994). The clusters identified by Bica et al. (2003) were observed in *J*, *H* and *K* bands by the Two Micron All Sky Survey (2MASS; Skrutskie et al. 1997) and the clusters identified by Goldader & Wynn-Williams (1994) were observed with the Near Infrared Camera and Multi-Object Spectrometer (NICMOS) on the University of Hawaii 2.2-m telescope. In addition to this catalogue, we also include the cluster associated with the H II region G49.2–0.3 from Kumar et al. (2004) based on *J*-, *H*- and *K*-band observations using the 3.8-m United Kingdom Infrared Telescope (UKIRT). This particular cluster was not catalogued by Bica et al. (2003) as it was not detected by 2MASS. Due to the improvement/depth of UKIRT Infrared Deep Sky Survey (UKIDSS) data in comparison to 2MASS, we inspected all the clusters within the Bica et al. (2003) catalogue using the UKIDSS Galactic Plane Survey data (Lucas et al. 2008)⁶ to improve confidence in using these clusters. The clusters used, after inspection in UKIDSS data, are given in Table 4. Unlike the clump catalogue presented in this paper, the clusters considered have no velocity information and so are used for spatial reference only. The locations of the clumps and young clusters are shown in Fig. 12.

In Fig. 12, we see that both the young clusters and supercritical clumps are distributed throughout the W51 GMC region although differences in locations are seen. The young clusters are found close to a line running through the HVS, with the majority (nine out of 14) found within the W51A region of the GMC. On inspection of the clumps close to the young clusters, we find these regions harbour warmer clumps than typical excitation temperatures above the median of the GMC (>25 K compared to a median of 12 K). We find that the supercritical clumps are located further away from this strip with this lack of apparent correlation between the locations of the supercritical clumps and clusters suggesting the young clusters have suppressed as opposed to induced nearby star formation.

From Fig. 12, we also see a notable absence of supercritical clumps within the W51A region, i.e. an apparent shift in the location of future star formation. This shift is reflected in the CFE whereby the W51 region has a CFE of 11 ± 1 per cent compared to the HVS that has a CFE of nearly a factor of 3 times greater than this, 29 ± 2 per cent. At first glance this idea appears to be inconsistent with an SCFE for the W51 region of 0.6 per cent and 0.1 per cent for the HVS. However, the considerable errors on these quantities ($0.6^{+2.6}_{-0.5}$ and $0.1^{+3.5}_{-0.1}$) means we cannot make any conclusive remarks about the future star formation potential of either the W51 region or the HVS in more detail. We do, however, see evidence of current star formation from the presence of multiple molecular outflows in the ^{12}CO HARP data cubes. This indicates a substantial component of present-day star formation in W51, and we will present a comprehensive study of these outflows in a subsequent publication.

Table 4. Clusters within the W51 region as used in Fig. 12.

RA	Dec.	Type ^a
19:22:15	+14:03:32	IRC
19:22:26	+14:06:54	IRC
19:23:14	+14:27:33	IRGr
19:23:19	+14:29:23	IRCC
19:23:29	+14:31:43	IRCC
19:23:33	+14:29:47	IRCC
19:23:41	+14:29:15	IRCC
19:23:43	+14:29:55	IRCC
19:23:42	+14:30:47	IRCC
19:23:43	+14:30:34	IRCC
19:23:40	+14:31:13	IRCC
19:23:48	+14:33:15	IRCC
19:23:51	+14:32:57	IRCC
19:23:02	+14:16:41	IRC ^b

^aAs denoted in Bica et al. (2003), where IRC, IRGr and IRCC are notation for infrared cluster, stellar group and infrared cluster candidate, respectively.

^bAs observed by Kumar et al. (2004).

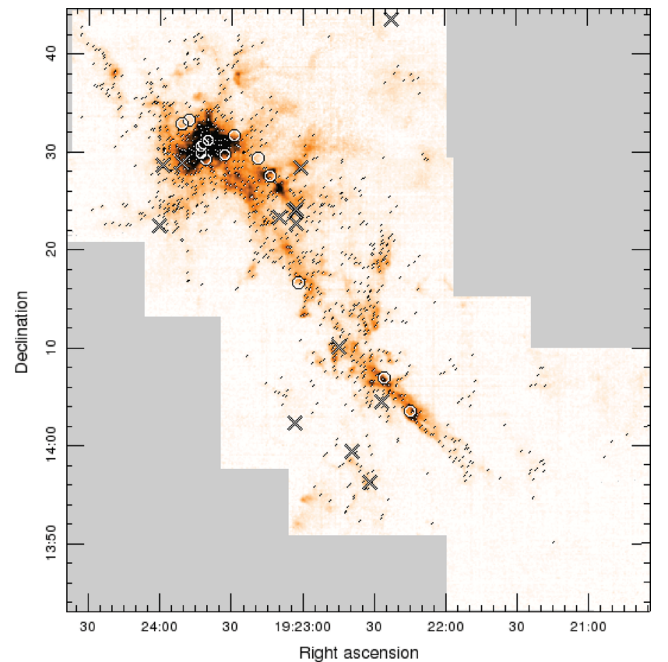


Figure 12. ^{13}CO (3–2) integrated intensity images of the W51 GMC region. Large crosses indicate the location of all supercritical clumps, small diamonds indicate the location of all subcritical clumps and large circles indicate the location of young clusters catalogued by Bica et al. (2003) and Kumar et al. (2004) as given in Table 4. Image excludes coverage on far right where emission is below 40 km s^{-1} as in Fig. 2.

Previous studies have suggested that the active star-forming nature of the W51 GMC is due to a collision between the W51 complex and the HVS (Pankonin, Payne & Terzian 1979; Arnal & Goss 1985; Carpenter & Sanders 1998; Okumura et al. 2001; Kang et al. 2010). This may explain the spread of young clusters over the GMC and the shift in star formation away from the W51A region; however, globally we see no spatial evidence suggesting that sequential star formation is taking place (Elmegreen 1998).

⁶ see http://surveys.roe.ac.uk:8080/wsa/gps_mosaic.jsp.

5 SUMMARY AND CONCLUSIONS

This paper presents a new catalogue of dense clumps within the W51 GMC that have been detected by HARP in ^{13}CO (3–2) and identified using the CLUMPFIND algorithm. To identify dense clumps, our method required detections to have a peak signal of 10σ in the ^{13}CO and a 3σ detection in C^{18}O . The clumps also have to contain a minimum of 16 pixels and have sizes greater than the telescope resolution in RA, Dec. and velocity ($\Delta\text{RA} \geq 14$ arcsec or $\Delta\text{Dec.} \geq 14$ arcsec or $\Delta v \geq 0.5 \text{ km s}^{-1}$). Clump emission was integrated down to a minimum contour level of 2σ to ensure that the maximum amount of clump emission was traced with a contour increment of 5σ used to distinguish between neighbouring clumps. From our catalogue of dense clumps identified, we find the following.

(i) A total of 1575 dense clumps are detected within the region mapped by HARP, and of these 1130 are associated with the W51 GMC.

(ii) The clumps have characteristic diameters of 1.0 pc (0.5–3.4 pc), excitation temperatures of 12 K (7–56 K), densities of $5.6 \times 10^{21} \text{ cm}^{-2}$ (7.4×10^{20} to $5.6 \times 10^{22} \text{ cm}^{-2}$), surface densities of 0.02 g cm^{-2} (0.002 – 0.19 g cm^{-2}) and masses of $90 M_{\odot}$ (10 – $1700 M_{\odot}$).

(iii) Surface densities are lower than expected (based on values outlined in Plume et al. 1997; McKee & Tan 2003; McKee & Ostriker 2007; Krumholz & McKee 2008), but are consistent with observations by Elia et al. (2010) and Roy et al. (2011), who find values down to 0.001 g cm^{-2} . Combined with our characteristic diameters of the order of parsecs, this result appears to agree with the sentiment of Roy et al. (2011), who theorize that these structures are extended massive reservoirs that have yet to be channelled by gravity into a higher surface density state.

(iv) The GMC has a large mass reservoir ($1.5 \times 10^5 M_{\odot}$) for future star formation with 1 per cent of the clumps by number (4 per cent by mass) found to be supercritical.

(v) A clump formation efficiency, CFE, of 14 per cent is determined for the W51 GMC, 11 per cent for the W51 complex and 29 per cent for the HVS. A look at this fraction in terms of supercritical clumps yields an SCFE of $0.5^{+2.3}_{-0.5}$ per cent for the W51 GMC. This indicates that the future star formation efficiency for the W51 GMC may diminish over time when compared to the current star formation efficiency reported by Okumura et al. (2000) of 2–8 per cent.

(vi) The CMD for the W51 GMC can be described by a single power law described by an exponent $\alpha = 2.4^{+0.2}_{-0.1}$. Both the W51 complex and the HVS are also best described by this single power law within the errors. This power law is consistent with the upper end of double power laws for other star-forming regions, the difference with the W51 GMC being that at such a large distance we are tracing larger and more massive structures and can only realistically fit a power law to higher mass clumps ($>200 M_{\odot}$) due to sample completeness.

(vii) It is found that the locations of supercritical clumps are spread throughout the W51 GMC with no evidence for sequential star formation. We tentatively suggest that future star formation will shift away from W51A, from the lack of supercritical clumps present compared to a high proportion of young clusters as identified by Bica et al. (2003) and Kumar et al. (2004).

Previous studies have presented the W51 GMC as region of starburst-like activity that has occurred within the past 3 Myr (Okumura et al. 2000; Kumar et al. 2004; Clark et al. 2009) throughout the entire complex (H II regions well distributed). From the data

presented within this paper, we remain unsure whether this is likely to continue. The caveat here is the fact that we are tracing the clumps only and activity within these clumps, on the scales of cores, may present a different picture of the star formation within the W51 GMC, although early results from a subsequent paper investigating molecular outflows within the GMC (using $^{12}\text{CO } J = 3-2$) indicate star formation is indeed ongoing within this GMC.

Future investigations of the W51 GMC will benefit from observations covered by the Herschel key programme Hi-GAL between 70 and $500 \mu\text{m}$ (Molinari et al. 2010b), with the first results presented by Molinari et al. (2010a) of $2^\circ \times 2^\circ$ centred on $l = 30^\circ$ and 59° indicating the real and exciting potential of Hi-GAL. Data from the Submillimetre Common-User Bolometer Array 2 ‘All Sky’ Survey, SASSy, at $850 \mu\text{m}$ (Thompson et al. 2007; Mackenzie et al. 2011) will complement Herschel data.

On a final note, we find that the W51 GMC has a mass of the same order of magnitude as other GMCs such as G305 (Hindson et al. 2010) and the Carina nebula (Preibisch et al. 2011). These too have been forming stars on similar time-scales (<5 Myr; Clark & Porter 2004); however, stark differences in their morphologies are indicative of their differing star-forming histories. Further studies are required to investigate these variations on individual GMC scales to provide deeper insight into GMC evolution with respect to their natal composition and also the star formation history.

ACKNOWLEDGMENTS

We thank the referee and Jennifer Hatchell for very constructive feedback that helped us to significantly improve our paper. We thank the STFC, the University of Hertfordshire and the staff at the Joint Astronomy Centre. This research has made use of NASA’s Astrophysics Data System. We would also like to acknowledge the JCMT (The James Clerk Maxwell Telescope is operated by The Joint Astronomy Centre on behalf of the Science and Technology Facilities Council of the United Kingdom, the Netherlands Organisation for Scientific Research and the National Research Council of Canada). This research used the facilities of the Canadian Astronomy Data Centre operated by the National Research Council of Canada with the support of the Canadian Space Agency. Finally, we would like to dedicate this paper to the memory of Louise Parsons.

REFERENCES

- Arnal E. M., Goss W. M., 1985, *A&A*, 145, 369
- Bate M. R., Bonnell I. A., 2005, *MNRAS*, 356, 1201
- Bica E., Dutra C. M., Soares J., Barbuy B., 2003, *A&A*, 404, 223
- Bonnell I. A., Bate M. R., 2006, *MNRAS*, 370, 488
- Bonnell I. A., Bate M. R., Zinnecker H., 1998, *MNRAS*, 298, 93
- Bonnell I. A., Smith R. J., Clark P. C., Bate M. R., 2011, *MNRAS*, 410, 2339
- Buckle J. V. et al., 2009, *MNRAS*, 399, 1026
- Buckle J. V. et al., 2010, *MNRAS*, 401, 204
- Carpenter J. M., Sanders D. B., 1998, *AJ*, 116, 1856
- Cavanagh B., Jennens T., Economou F., Currie M. J., 2008, *Astron. Nachr.*, 329, 295
- Clark J. S., Porter J. M., 2004, *A&A*, 427, 839
- Clark J. S., Davies B., Najarro F., MacKenty J., Crowther P. A., Messineo M., Thompson M. A., 2009, *A&A*, 504, 429
- Crowther P. A., Schnurr O., Hirschi R., Yusuf N., Parker R. J., Goodwin S. P., Kassim H. A., 2010, *MNRAS*, 408, 731
- Curtis E. I., Richer J. S., 2010, *MNRAS*, 402, 603
- Curtis E. I., Richer J. S., Buckle J. V., 2010, *MNRAS*, 401, 455
- Elia D. et al., 2010, *A&A*, 518, L97

- Elmegreen B. G., 1998, in Woodward C. E., Shull J. M., Thronson H. A., Jr, eds, *ASP Conf. Ser. Vol. 148, Origins. Astron. Soc. Pac.*, San Francisco, p. 150
- Figuerêdo E., Blum R. D., Damineli A., Conti P. S., Barbosa C. L., 2008, *AJ*, 136, 221
- Frerking M. A., Langer W. D., Wilson R. W., 1982, *ApJ*, 262, 590
- Garden R. P., Hayashi M., Hasegawa T., Gatley I., Kaifu N., 1991, *ApJ*, 374, 540
- Goldader J. D., Wynn-Williams C. G., 1994, *ApJ*, 433, 164
- Hindson L., Thompson M. A., Urquhart J. S., Clark J. S., Davies B., 2010, *MNRAS*, 408, 1438
- Kang M., Bieging J. H., Povich M. S., Lee Y., 2009, *ApJ*, 706, 83
- Kang M., Bieging J. H., Kulesa C. A., Lee Y., Choi M., Peters W. L., 2010, *ApJS*, 190, 58
- Koo B.-C., 1999, *ApJ*, 518, 760
- Kramer C., Stutzki J., Rohrig R., Corneliussen U., 1998, *A&A*, 329, 249
- Kroupa P., 2001, *MNRAS*, 322, 231
- Krumholz M. R., McKee C. F., 2008, *Nat*, 451, 1082
- Kumar M. S. N., Kamath U. S., Davis C. J., 2004, *MNRAS*, 353, 1025
- Kundu M. R., Velusamy T., 1967, *Ann. Astrophys.*, 30, 59
- Ladd E. F., Fuller G. A., Deane J. R., 1998, *ApJ*, 495, 871
- Lucas P. W. et al., 2008, *MNRAS*, 391, 136
- McKee C. F., Ostriker E. C., 2007, *ARA&A*, 45, 565
- McKee C. F., Tan J. C., 2003, *ApJ*, 585, 850
- Mackenzie T. et al., 2011, *MNRAS*, 415, 1950
- MacLaren I., Richardson K. M., Wolfendale A. W., 1988, *ApJ*, 333, 821
- Maíz Apellániz J., Úbeda L., 2005, *ApJ*, 629, 873
- Molinari S. et al., 2010a, *A&A*, 518, L100
- Molinari S. et al., 2010b, *PASP*, 122, 314
- Moore T. J. T., Bretherton D. E., Fujiyoshi T., Ridge N. A., Allsopp J., Hoare M. G., Lumsden S. L., Richer J. S., 2007, *MNRAS*, 379, 663
- Motte F., Andre P., Neri R., 1998, *A&A*, 336, 150
- Mufson S. L., Liszt H. S., 1979, *ApJ*, 232, 451
- Myers P. C., Linke R. A., Benson P. J., 1983, *ApJ*, 264, 517
- Myers P. C., Dame T. M., Thaddeus P., Cohen R. S., Silverberg R. F., Dwek E., Hauser M. G., 1986, *ApJ*, 301, 398
- Nutter D., Ward-Thompson D., 2007, *MNRAS*, 374, 1413
- Okumura S., Mori A., Nishihara E., Watanabe E., Yamashita T., 2000, *ApJ*, 543, 799
- Okumura S., Miyawaki R., Sorai K., Yamashita T., Hasegawa T., 2001, *PASJ*, 53, 793
- Pankonin V., Payne H. E., Terzian Y., 1979, *A&A*, 75, 365
- Parmentier G., Goodwin S. P., Kroupa P., Baumgardt H., 2009, *Ap&SS*, 324, 327
- Pascale E. et al., 2008, *ApJ*, 681, 400
- Plume R., Jaffe D. T., Evans N. J., II, Martin-Pintado J., Gomez-Gonzalez J., 1997, *ApJ*, 476, 730
- Preibisch T., Schuller F., Ohlendorf H., Pekruhl S., Menten K. M., Zinnecker H., 2011, *A&A*, 525, A92
- Rathborne J. M., Johnson A. M., Jackson J. M., Shah R. Y., Simon R., 2009, *ApJS*, 182, 131
- Reid M. A., Wilson C. D., 2006a, *ApJ*, 644, 990
- Reid M. A., Wilson C. D., 2006b, *ApJ*, 650, 970
- Reid M. A., Wadsley J., Petitsclerc N., Sills A., 2010, *ApJ*, 719, 561
- Rohlfs K., Wilson T. L., 2004, *Tools of Radio Astronomy*. Springer, Berlin
- Roy A. et al., 2011, *ApJ*, 727, 114
- Russeil D., 2003, *A&A*, 397, 133
- Salpeter E. E., 1955, *ApJ*, 121, 161
- Sato F., 1973, *PASJ*, 25, 135
- Sato M., Reid M. J., Brunthaler A., Menten K. M., 2010, *ApJ*, 720, 1055
- Schneider N., Brooks K., 2004, *Publ. Astron. Soc. Australia*, 21, 290
- Shi H., Zhao J., Han J. L., 2010, *ApJ*, 710, 843
- Simpson R. J., Nutter D., Ward-Thompson D., 2008, *MNRAS*, 391, 205
- Skrutskie M. F. et al., 1997, in Garzon F., Epchtein N., Omont A., Burton B., Persi P., eds, *Astrophysics and Space Science Library Vol. 210, The Impact of Large Scale Near IR Sky Surveys*. Kluwer, Dordrecht, p. 25
- Smith R. J., Clark P. C., Bonnell I. A., 2008, *MNRAS*, 391, 1091
- Sollins P. K., Zhang Q., Ho P. T. P., 2004, *ApJ*, 606, 943
- Solomon P. M., Rivolo A. R., Barrett J., Yahil A., 1987, *ApJ*, 319, 730
- Störzer H., Zielinsky M., Stutzki J., Sternberg A., 2000, *A&A*, 358, 682
- Thompson M. A. et al., 2007, preprint
- Ward-Thompson D. et al., 2007, *PASP*, 119, 855
- Westerhout G., 1958, *Bull. Astron. Inst. Netherlands*, 14, 215
- Williams J. P., de Geus E. J., Blitz L., 1994, *ApJ*, 428, 693
- Williams J. P., Blitz L., McKee C. F., 2000, in Mannings V., Boss A. P., Russell S. S., eds, *Protostars and Planets IV*. Univ. Arizona Press, Tucson, p. 97
- Wilson T. L., 1999, *Rep. Progress Phys.*, 62, 143
- Wilson T. L., Rood R., 1994, *ARA&A*, 32, 191
- Wilson R. W., Langer W. D., Goldsmith P. F., 1981, *ApJ*, 243, L47
- Xu Y., Reid M. J., Menten K. M., Brunthaler A., Zheng X. W., Moscadelli L., 2009, *ApJ*, 693, 413
- Yorke H. W., Sonnhalter C., 2002, *ApJ*, 569, 846
- Zapata L. A., Ho P. T. P., Schilke P., Rodríguez L. F., Menten K., Palau A., Garrod R. T., 2009, *ApJ*, 698, 1422

SUPPORTING INFORMATION

Additional Supporting Information may be found in the online version of this article.

Table 1. Properties for the 445/1575 clumps identified by CLUMPFIND within the region observed by HARP with velocities $< 56 \text{ km s}^{-1}$.

Table 2. Properties for the 1130/1575 clumps identified by CLUMPFIND associated with the W51 GMC.

Please note: Wiley-Blackwell are not responsible for the content or functionality of any supporting materials supplied by the authors. Any queries (other than missing material) should be directed to the corresponding author for the article.

This paper has been typeset from a \LaTeX file prepared by the author.